

RIS-Enabled Self-Localization with FMCW Radar

Hyowon Kim, *Member, IEEE*, Navid Amani, Musa Furkan Keskin, *Member, IEEE*,
 Zhongxia Simon He, *Senior Member, IEEE*, Jorge Gil,
 Gonzalo-Seco Granados, *Fellow, IEEE*, and Henk Wymeersch, *Fellow, IEEE*

Abstract—In the upcoming vehicular networks, reconfigurable intelligent surfaces (RISs) are considered as a key enabler of user self-localization without the intervention of the access points (APs). In this paper, we investigate the feasibility of RIS-enabled self-localization with no APs. We first develop a digital signal processing (DSP) unit for estimating the geometric parameters such as the angle, distance, and velocity and for RIS-enabled self-localization. Second, we set up an experimental testbed consisting of a Texas Instrument frequency modulated continuous wave (FMCW) radar for the user and SilversIMA module for the RIS. Our results confirm the validity of the developed DSP unit and demonstrate the feasibility of RIS-enabled self-localization.

Index Terms—Channel parameters estimation, frequency modulated continuous wave radar, localization, reconfigurable intelligent surface.

I. INTRODUCTION

Navigation, especially in unknown areas without access to global navigation satellite systems (GNSS), presents a significant challenge [1], [2]. Simultaneous localization and mapping (SLAM) offers a promising solution by allowing a system to map and localize itself simultaneously in real-time [3], [4]. However, traditional SLAM systems heavily rely on optical sensors like cameras or LiDAR, which are limited in vision-denied environments—conditions such as smoke-filled rooms, darkness, or areas with poor visibility [5]–[7]. These are conditions commonly encountered by first responders during rescue missions or in industrial environments [7].

To address these limitations, frequency modulated continuous wave (FMCW) radar has emerged as a viable alternative [8], [9]. Unlike optical sensors, FMCW radar can operate reliably under various weather conditions, including fog, rain, or dust [10]. It has already been successfully adopted for autonomous vehicles and robotics [11], making it a potential solution for SLAM in harsh or low-visibility environments [12]. Radar odometry enhances SLAM by analyzing features in the environment, such as static objects like walls, through consecutive radar scans. By matching environmental features across several radar scans radar odometry can estimate the movement of a vehicle or robot [13].

Rather than relying solely on natural features for localization, we propose to leverage reconfigurable intelligent sur-

H. Kim is with the Department of Electronics Engineering, Chungnam National University, Daejeon, South Korea (email: hyowon.kim@cnu.ac.kr). M. F. Keskin, N. Amani and H. Wymeersch are with the Department of Electrical Engineering, Chalmers University of Technology, Gothenburg, Sweden (email: furkan, anavid, henkw@chalmers.se). Z. S. He is with Chalmers Industriteknik, Gothenburg, Sweden (email: simon.he@chalmersindustriteknik.se). J. Gil is with the Department of Architecture and Civil Engineering, Chalmers University of Technology, Gothenburg, Sweden (email: jorge.gil@chalmers.se). G. Seco Granados is with the Universitat Autònoma de Barcelona, Barcelona, Spain (email: gonzalo.seco@uab.cat)

This work was supported by the Chalmers Transport Area of Advance, the Swedish Research Council grant 2022-03007 and 2023-05184.



Fig. 1. Considered scenario where an FMCW radar is localized using an RIS. RISs are used as artificial landmarks to enhance *radar self-localization* in SLAM applications. Although RISs have been extensively studied in the context of radar-like sensing of *passive* objects in monostatic [14]–[19], bistatic [20]–[22] and multistatic [23] configurations, their use in self-localization of an *active* transmitting device (i.e., a full-duplex radar) remains relatively under-explored, e.g., [24], [25]. RISs as artificial landmarks can be strategically placed in the environment, offering consistent and reliable reference points for radar systems [24], [26]. Moreover, such RIS-assisted self-localization solution obviates the need for additional costly infrastructure such as access points (APs) or base stations (BSs) [27], [28] and provides a cost-effective strategy to implement radar-based SLAM [25]. While RIS-assisted self-localization has been theoretically investigated in [24], [25], its feasibility has not been demonstrated in a real-world experimental setup.

In this paper, we aim to bridge this gap by designing an experimental setup for RIS-aided self-localization of a monostatic FMCW radar (shown in Fig. 1), accompanied by algorithms for RIS beam scanning, distance and AOD estimation for localization, and a simulator calibrated to match experimental results and evaluate performance under a wide range of realistic conditions. Our specific contributions are: (i) We develop a method tailored for RIS-aided self-localization, allowing real-time estimation of critical geometric parameters such as angle of departure, distance, and velocity in a monostatic radar configuration; (ii) We construct a comprehensive experimental testbed, incorporating an FMCW radar from Texas Instruments [29] to emulate the UE and a transceiver from SilversIMA [30] to emulate the RIS, to validate the proposed self-localization approach under realistic conditions; (iii) We evaluate the feasibility and accuracy of RIS-enabled self-localization through experimental data analysis, and develop a simulator calibrated with this data to investigate system performance under various scenarios, including changes in transmit power, RIS sweep step size, and RIS array dimensions.

II. SYSTEM MODEL

We consider a full-duplex user equipment (UE) and a passive RIS. The RIS is equipped with a uniform planar array (UPA) composed of $N_{\text{RIS}} = N_{\text{RIS}}^{\text{az}} \times N_{\text{RIS}}^{\text{el}}$ radiating elements,

which lies on the xz plane, and the UE is equipped with a single antenna. Both UE and RIS are static. The UE location is denoted by \mathbf{x}_{UE} . The geometric center of elements at the RIS is denoted by \mathbf{x}_{RIS} and the location of the n -th element is denoted by $\mathbf{x}_{\text{RIS}}^n$.

The UE transmits the chirp signals, and the RIS reflects the signals by controlling the RIS phases, performing a sweeping action across the angular range. The other surrounding objects reflect the transmitted signals. Then, the UE receives multipath due to reflection or scattering in the propagation environment consisting of the RIS and other objects. The analog-to-digital converter (ADC) sample, chirp, RIS sweep angle, and signal path are respectively indexed by n , k , m , and l . The beat signal at the intermediate frequency (IF) for the m -th RIS sweep angle is denoted by \mathbf{Y}_m whose element $[\mathbf{Y}_m]_{n,k}$ indicates the signal on the n -th sample for each k -th chirp, given by [10]

$$[\mathbf{Y}_m]_{n,k} = \gamma_0 e^{-j2\pi(S\tau_0 + f_c\nu_0)nT_s} e^{-j2\pi f_c\nu_0 kT} \mathbf{a}^\top(\boldsymbol{\theta}) \boldsymbol{\Omega}_m \mathbf{a}(\boldsymbol{\theta}) + \sum_{l=1}^L \gamma_l e^{-j2\pi(S\tau_l + f_c\nu_l)nT_s} e^{-j2\pi f_c\nu_l kT} + w_{n,k,m}, \quad (1)$$

where the index $l = 0$ indicates the reflected signals from the RIS and $l > 0$ for the reflected signals from the other objects, the total number of signal paths is $L + 1$, γ_l is the complex path gain, $\mathbf{a}(\boldsymbol{\theta}) \triangleq \exp(j\mathbf{X}_{\text{RIS}}^\top \mathbf{g}(\boldsymbol{\theta}))$ denotes the array vector at the RIS with $\boldsymbol{\theta} \triangleq [\theta^{\text{az}}, \theta^{\text{el}}]^\top$ being the angle-of-arrival (AoA) and angle-of-departure (AoD) at the RIS,¹ $\mathbf{g}(\boldsymbol{\theta}) \triangleq \frac{2\pi}{\lambda} [\cos(\theta^{\text{az}}) \sin(\theta^{\text{el}}), \sin(\theta^{\text{az}}) \sin(\theta^{\text{el}}), \cos(\theta^{\text{el}})]^\top$ is the wavenumber vector, $\lambda = c/f_c$ is the wavelength, c is the speed of light, f_c is the carrier frequency, $\mathbf{X}_{\text{RIS}} \triangleq [\mathbf{x}_{\text{RIS}}^1, \dots, \mathbf{x}_{\text{RIS}}^{N_{\text{RIS}}}]$, $\boldsymbol{\Omega}_m = \text{diag}(\boldsymbol{\omega}_m)$ is the RIS phase matrix, and $\boldsymbol{\omega}_m \triangleq \exp(-2j\mathbf{X}_{\text{RIS}}^\top \mathbf{g}(\boldsymbol{\phi}_m))$ is the RIS phase profile vector whose elements lie on the unit circle with $\boldsymbol{\phi}_m \triangleq [\phi_m^{\text{az}}, \phi_m^{\text{el}}]^\top$ being the parameter vector corresponding to the m -th sweep angle at the RIS. During m -th sweep angle, i.e., seen as a frame, K chirps are transmitted, and each chirp consists of N ADC samples. Furthermore, $S = B/T$ denotes the chirp slope, B is the sweep bandwidth, T is the chirp duration, T_s is the sample duration, $\tau_l = 2d_l/c$ is the round-trip time delay, d_l is the true distance between the UE and object producing the l -th reflection, whose radial velocity is denoted by ν_l , and hence $\nu_l = 2v_l/c$ is the corresponding Doppler shift, $w_{n,k,m} \sim \mathcal{CN}(0, \sigma_N^2)$ is the complex Gaussian noise, and σ_N^2 is the signal noise covariance.

III. RIS-ENABLED SELF-LOCALIZATION

This section describes the signal processing at the FMCW receiver.

A. Delay and Doppler Spectrum

To jointly estimate the distance and radial velocity, we apply the two-dimensional (2D) discrete Fourier transform (DFT) to the beat signal (1) for the sample and chirp dimensions, generating the FMCW delay-Doppler spectrum as described below. We first utilize windowing on the signals

$$\tilde{\mathbf{Y}}_m = \mathbf{w}_N \mathbf{w}_K^\top \odot \mathbf{Y}_m, \quad (2)$$

where \mathbf{w}_A is the window vector with A samples and \odot denotes the Hadamard (element-wise) product. To increase the estimation accuracy in 2D DFT, we adopt the zero padding

$$\mathbf{Y}'_m = \begin{bmatrix} \tilde{\mathbf{Y}}_m & \mathbf{0}_{N \times (K_{\text{DFT}} - K)} \\ \mathbf{0}_{(N_{\text{DFT}} - N) \times K} & \mathbf{0}_{(N_{\text{DFT}} - N) \times (K_{\text{DFT}} - K)} \end{bmatrix}, \quad (3)$$

where N_{DFT} and K_{DFT} are respectively the number of DFT samples for ADC samples and chirps. For the different RIS beam sweep angles, i.e., $m = 1, \dots, M$, we generate the delay-Doppler map with the 2D DFT

$$z_m(\tau, \nu) = \sum_{k=0}^{K_{\text{DFT}}-1} \sum_{n=0}^{N_{\text{DFT}}-1} [\mathbf{Y}'_m]_{n,k} e^{j2\pi S\tau n T_s} e^{j2\pi f_c \nu k T}. \quad (4)$$

B. Geometric Parameter Estimation

We estimate the following geometric parameters: AoD from the RIS, distance between the UE and RIS, and Doppler shift at the UE. The geometric parameters are estimated as follows. First, we determine the delay and Doppler pairs for the different RIS beam sweep angles, i.e., $m = 1, \dots, M$,

$$(\tau_m, \nu_m) = \underset{\tau, \nu}{\text{argmax}} |z_m(\tau, \nu)|^2, \quad (5)$$

Second, we estimate the AoD at the RIS by RIS beam sweeping. The received power for each beam is determined by $\hat{m} = \underset{m}{\text{argmax}} P_{\text{ave},m}$, where

$$P_{\text{ave},m} = \frac{1}{2\Delta} \int_{\tau_m - \Delta}^{\tau_m + \Delta} |z_m(\tau, \nu_m)|^2 d\tau, \quad (6)$$

where Δ is a design parameter. The estimated AoD $\hat{\boldsymbol{\theta}} \triangleq [\hat{\theta}^{\text{az}}, \hat{\theta}^{\text{el}}]^\top$ is the \hat{m} -th RIS beam $\hat{\boldsymbol{\theta}} = \boldsymbol{\phi}_{\hat{m}}$. Finally, the distance and Doppler are estimated by selecting \hat{m} -th delay and Doppler pair, i.e., $(\hat{\tau}, \hat{\nu}) = (\tau_{\hat{m}}, \nu_{\hat{m}})$, and the estimated distance and Doppler are determined by $\hat{d} = \hat{\tau}c/2$ and $\hat{v} = \hat{\nu}c/2$, respectively.

C. Localization

We estimate the UE location by exploiting the estimated distance \hat{d} and RIS AoD $\hat{\boldsymbol{\theta}}$. The estimated UE location is

$$\mathbf{x}_{\text{UE}} = \mathbf{x}_{\text{RIS}} + \begin{bmatrix} \hat{d} \cos(\hat{\theta}^{\text{az}}) \sin(\hat{\theta}^{\text{el}}) \\ \hat{d} \sin(\hat{\theta}^{\text{az}}) \sin(\hat{\theta}^{\text{el}}) \\ \hat{d} \cos(\hat{\theta}^{\text{el}}) \end{bmatrix}. \quad (7)$$

IV. EXPERIMENTAL AND SIMULATION SETUP

A. Experimental Testbed

Our experimental testbed for RIS-enabled self-localization is depicted in Fig. 2. We deploy the UE and RIS in a large hall, separated by a clear line-of-sight (LOS) path at a distance of approximately 14 meters, as shown in Fig. 2a. Both are facing each other and located at the same height, indicating that the AoD at the RIS is set to $\boldsymbol{\theta} = [0, 0]^\top$. We emulate the UE by the FMCW radar evaluation kit (AWR6843ISK) from Texas Instruments (TI) (see, Fig. 2b), and RIS by the mmWave wireless communication module from SiversIMA (see, Fig. 2c) to mimic RIS beamforming capabilities. Both operate at the frequency of 60 GHz. To complement the radar module at the UE, we deploy the DCA1000EVM for real-time data capture and streaming. This configuration allows us to seamlessly collect radar data for further processing. We developed an in-house DSP unit using MATLAB, which processes the radar-captured data to extract the relevant experimental results. The

¹In monostatic systems, the AoA at an object is the same as the AoD.

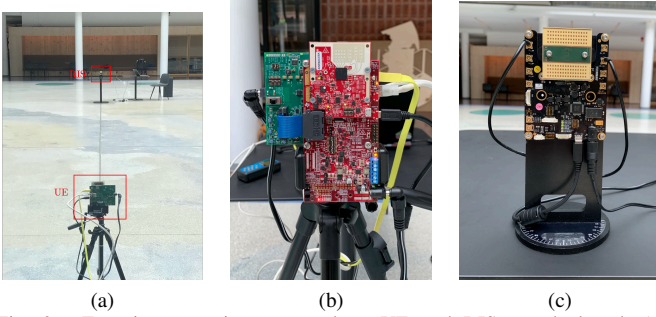


Fig. 2. Experiment environment, where UE and RIS are deployed: (a) displacement of UE and RIS; (b) UE; and (c) RIS.

SiversIMA module is equipped with separate transmit (Tx) and receive (Rx) channels, where each consists of 16×4 antenna elements, as illustrated in Fig. 2c, which allows it to receive radar chirps from the radar module and transmit them back in a specific direction. The beam-steering functionality of the RIS enables directional re-transmissions within an angle range of -45 to $+45$ degrees relative to its broadside, making it highly adaptable for our purposes. During the experiment, the UE continuously transmits FMCW chirps, which are received by the Rx channels of the RIS. These signals are then re-transmitted by the RIS at varying scan angles, covering the entire RIS angular range ϕ_m^{az} from -45 to 45 degrees in 1.5 -degree increments² and $\phi_m^{el} = 0^\circ$. While this process takes place, the UE captures samples of the reflected signals at each scan angle. This experimental method allows us to measure the average power at the radar for different beam-steering angles on the RIS side, $P_{ave,m}$ of (6) in dBm. By systematically varying the angles and recording the response of the radar, we estimate the RIS AoD that maximizes the average power $P_{ave,m}$. Treating the RIS as an artificial landmark with a known location allows the radar to accurately self-localize, while simultaneously generating environmental images for mapping purposes.

B. Simulation Setup

To validate the designed signal model of (1) and the proposed RIS-enabled self-localization method in Sec. III, we construct a simulator of our experimental testbed in the MATLAB environment. The goal is to harness the experimental results for calibrating the simulator, which are then employed to investigate performance under a rich set of conditions that cannot be tested with experiments. Instead of real-time signal capturing and streaming, we artificially generate the noisy signal data that follows the received signal model (1). The squared amplitude of complex path gain for the targets (i.e., $l > 0$) is $|\gamma_l|^2 = PG_{\text{trx}}S_{\text{RCS}}^l\lambda^2/((4\pi)^3d_l^4)$, where P is the transmit power, G_{trx} is the combined transmit and receive antenna gain, S_{RCS}^l is the radar cross section (RCS) of the objects that producing the signal reflection. As to the complex

²To emulate the RIS beam-steering process with separate Tx and Rx arrays, the Tx beamforming vector at the m -th sweep angle is $\omega_m^{\text{Tx}} = \exp(-j\mathbf{X}_{\text{Tx}}^T\mathbf{g}(\phi_m))$, defined with the RIS phase matrix of (1). Since in our experiment the RIS is located at the boresight of the UE for maximum reception, its receive beam is always directed toward the UE and does not change with the Tx beam scanning. Consequently, the Rx beamforming vector is $\omega_m^{\text{Rx}} = \exp(-j\mathbf{X}_{\text{Rx}}^T\mathbf{g}(\theta))$. Due to identical arrays, we have $\mathbf{X}_{\text{Tx}} = \mathbf{X}_{\text{Rx}}$.

TABLE I
THE SIMULATION PARAMETERS USED IN THE PERFORMANCE EVALUATIONS.

Parameter	Value
RIS array size	$N_{\text{RIS}} = 64 (16 \times 4)$
Transmission power	$P = 20$ dBm
Combined Tx and Rx antenna gain	$G_{\text{trx}} = 4.7712$ dBi
RCS of the targets (for $l > 0$)	$S_{\text{RCS}}^l = 19$ m ²
Amplification and loss factor	$\zeta = 45.532$ dB
Number of chirps	$K = 128$
Number of ADC samples	$N = 600$
Chirp duration	$T = 50$ ms
Sweep bandwidth	$B = 3.4345$ GHz
IF bandwidth	$B_{\text{IF}} = 10$ MHz
Carrier frequency	$f_c = 60$ GHz
Wavelength	$\lambda = 0.005$ m
Signal noise covariance	$\sigma_N^2 = -63.64$ dBm
Loop-back delay at the RIS	$\tau_{\text{RB}} = 1.78$ ns
Number of DFT samples	$N_{\text{DFT}} = 1199, K_{\text{DFT}} = 4793$
UE position	$\mathbf{x}_{\text{UE}} = [0, 0]^T$
RIS position	$\mathbf{x}_{\text{RIS}} = [0, 13.38]^T$

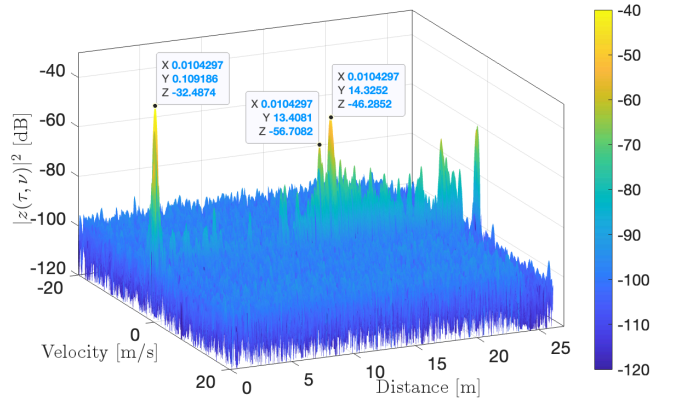


Fig. 3. Three largest peaks in 2D distance and velocity spectrum with the experiment data, obtained by (4) at the m -th RIS sweep angle corresponding to $\phi = [0^\circ, 0^\circ]^T$.

gain of the RIS loopback path ($l = 0$), it involves the impact of both amplification factors due to the active nature of the RIS [31] and the losses incurred during loopback from receive to transmit path in the active RIS: $\zeta = L_{\text{loss}}\alpha_{\text{RIS}}$, where α_{RIS} is the amplification factor common to all the RIS elements [31], [32] and L_{loss} is the loopback loss, both representing unitless quantities. Hence, the squared amplitude of the complex gain of the RIS loopback path can be expressed as [32], [33]

$$|\gamma_0|^2 = PG_{\text{trx}}|\gamma_{\text{UR}}|^2\zeta|\gamma_{\text{RU}}|^2, \quad (8)$$

where γ_{UR} and γ_{RU} denote the gains of the UE-RIS path and the RIS-UE radar path, respectively. We have [32] $|\gamma_{\text{UR}}|^2 = |\gamma_{\text{RU}}|^2 = \lambda^2/(4\pi d_0)^2$, where d_0 is the distance between the UE and the RIS. In the computation of average power (6), the design parameter Δ of (6) is set to 0.33 ns, the time delay corresponding to the distance 0.1 m. We utilize the Hann window function, and the a -th sample of the Hann window vector is $\mathbf{w}_A(a) = \sin^2(a\pi/A)$, where A is the number of samples. To consider the re-transmission process at the RIS, we adopt the loop-back delay τ_{RB} , and the estimated distance is computed by $\hat{d} = (\hat{\tau} - \tau_{\text{RB}})c/2$. The simulation parameters are summarized in Table I. The results are averaged over 1000 Monte Carlo simulation runs.

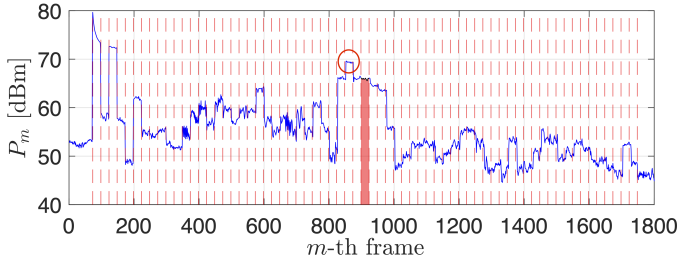


Fig. 4. Example of the AoD estimation ($\hat{\phi} = [-3^\circ, 0^\circ]^\top$ and $\phi = [0^\circ, 0^\circ]^\top$ corresponding to the frames marked by the red circle (estimates) and highlighted by the red bar (true), respectively).

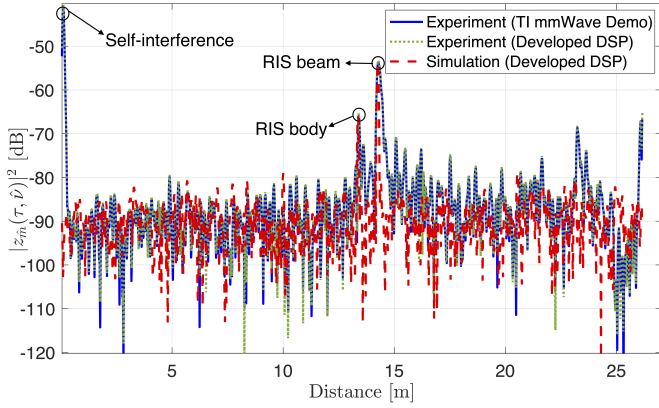


Fig. 5. Comparison of 1D distance profile results with the experiment data by the TI mmWave kit (solid line) and by the proposed parameter estimation method (dotted line), and simulation data by the designed signal model and proposed estimation method (dashed line), at $\nu \approx 0$ and $\phi = [0^\circ, 0^\circ]^\top$ corresponding to the \hat{m} -th RIS sweep angle.

V. RESULTS AND DISCUSSIONS

A. Experimental Results

Utilizing the collected experimental data in the testbed, we investigate the 2D distance and velocity spectrum, obtained by (4) at the RIS sweep angle corresponding to $\phi_m = [0, 0]^\top$, shown in Fig. 3. From the 2D spectrum, we see the first three largest peaks, where the first is the self-interference due to the Tx antenna leakage to Rx in monostatic (co-located) radars [34], the second by the physical reflection by the RIS, and the third by the retransmitted signal at the RIS. Therefore, we filter out the first peak and then exploit the parameter estimation method (Sec. III-B).

Fig. 4 shows the average power over the frames of (6), to estimate the AoD. The true AoD is $\phi = [0^\circ, 0^\circ]^\top$ corresponds to the frames highlighted by the red bar, and estimated AoD $\hat{\phi} = [-3^\circ, 0^\circ]^\top$ corresponds to the frames marked by the red circle. The average power fluctuates sharply in the initial few hundred frames, then gradually increases, and eventually gradually decreases after passing about the midpoint of the frames. This behavior is attributed to the RIS being turned on and off repeatedly during the initial few hundred frames for synchronization purposes, followed by the beam-steering sweep with the angular range from -45° (starting at the 150-th frame) to 45° in increments of 1.5° .

B. Simulation Results and Extrapolation

To validate the developed DSP unit using MATLAB including the formulated signal model (1) and the proposed geometric parameters estimation method (Sec. III-B), in Fig. 5,

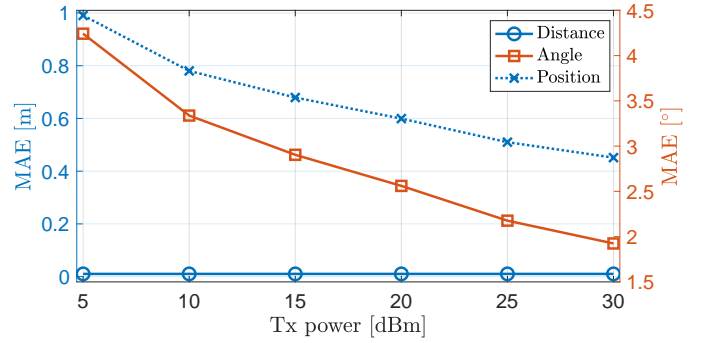


Fig. 6. MAEs of distance, angle, and position estimates with the different Tx powers.

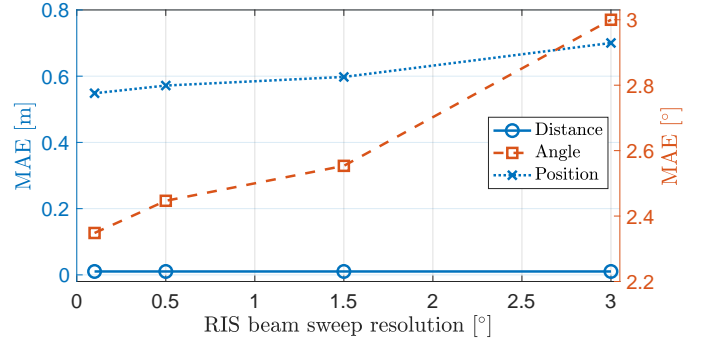


Fig. 7. MAEs of distance, angle, and position estimates with the different RIS beam sweep resolutions.

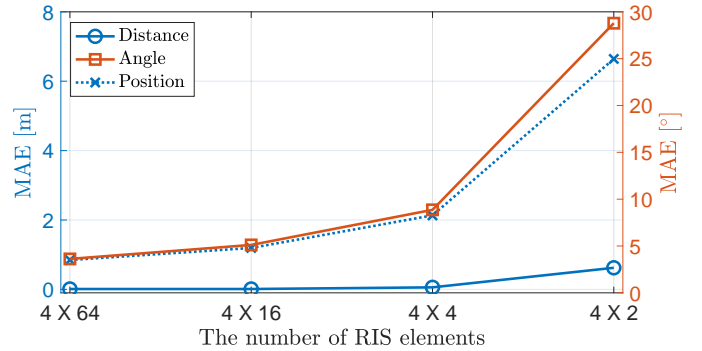


Fig. 8. MAEs of distance, angle, and position estimates with the different number of RIS elements.

we compare the 1D distance profile results, at $\nu \approx 0$ and $\theta = [0, 0]^\top$. The experiment data is analyzed by the TI mmWave radar (solid line) and by the proposed parameter estimation method (dotted line), which is also applied to the simulation data (dashed line). In the dashed line, the first peak that originated from the reflected signal from the UE itself is absent as this self-interference is not modeled in the simulated data. We demonstrate that the developed DSP is valid as the solid line matches the dotted line, and the dashed line has the same two peaks corresponding to physical reflection at the RIS and retransmitted signal at the RIS, as the solid and dotted lines.

Figs. 6–8 show the geometric parameters and positioning estimation errors with the different setup configurations. Fig. 6 presents the results with the different Tx powers. The distance estimation error does not vary for the range of Tx power values for which the peaks of the spectrum can be resolved in the distance dimension with a fixed distance search grid ($N_{\text{DFT}} = 1199$) on the distance profile. We see the

smaller AOD error with the larger Tx power. Due to the smaller AOD error with the larger Tx power, while maintaining the same distance errors, the positioning error also decreases as the Tx power increases. Fig. 7 shows the results with various RIS beam sweep resolutions. The fine beam leads to a smaller AOD estimation error while maintaining the distance estimation error due to the resolvable peaks with a fixed distance search grid on the distance profiles. Therefore, the positioning error decreases with the fine RIS beam sweep resolution. Fig. 8 presents the results with the different number of RIS elements. The distance estimation error also decreases with the larger number of RIS elements. This happens because the two peaks corresponding to physical reflection at the RIS and re-transmitted signal at the RIS are resolvable with the larger number of RIS elements. The AOD estimation error decreases as the number of RIS elements increases. Therefore, the positioning error decreases with the large number of RIS elements.

VI. CONCLUSIONS

In this paper, we demonstrated the feasibility of RIS-enabled self-localization without AP intervention through both experimental and simulation results. In the experimental testbed, we assessed the developed DSP unit by comparing the 1D distance profile with the TI mmWave radar evaluation kit. We confirmed the validity of our designed signal model, which adheres to the deterministic model, in the signal propagation environment of the 60 GHz FMCW radar. For future work, we plan to explore the feasibility of multiple target tracking and SLAM, with the assistance of RISs.

REFERENCES

- [1] K.-W. Chiang *et al.*, "Seamless navigation and mapping using an INS/GNSS/grid-based SLAM semi-tightly coupled integration scheme," *Information Fusion*, vol. 50, pp. 181–196, 2019.
- [2] G. He *et al.*, "An integrated GNSS/LiDAR-SLAM pose estimation framework for large-scale map building in partially gnss-denied environments," *IEEE Transactions on Instrumentation and Measurement*, vol. 70, pp. 1–9, 2021.
- [3] H. Durrant-Whyte *et al.*, "Simultaneous localization and mapping: Part I," *IEEE Robot. Autom. Mag.*, vol. 13, no. 2, pp. 99–110, Jun. 2006.
- [4] T. Bailey *et al.*, "Simultaneous localization and mapping (SLAM): Part II," *IEEE Robot. Autom. Mag.*, vol. 13, no. 3, pp. 108–117, Sep. 2006.
- [5] B. Amjad *et al.*, "Radio SLAM: A review on radio-based simultaneous localization and mapping," *IEEE Access*, vol. 11, pp. 9260–9278, 2023.
- [6] H. A. G. C. Premachandra *et al.*, "UWB radar SLAM: An anchorless approach in vision denied indoor environments," *IEEE Robotics and Automation Letters*, vol. 8, no. 9, pp. 5299–5306, 2023.
- [7] J. M. Santos *et al.*, "A sensor fusion layer to cope with reduced visibility in SLAM," *Journal of Intelligent & Robotic Systems*, vol. 80, pp. 401–422, 2015.
- [8] A. Venon *et al.*, "Millimeter wave FMCW radars for perception, recognition and localization in automotive applications: A survey," *IEEE Transactions on Intelligent Vehicles*, vol. 7, no. 3, pp. 533–555, 2022.
- [9] S. M. Patole *et al.*, "Automotive radars: A review of signal processing techniques," *IEEE Signal Processing Magazine*, vol. 34, no. 2, pp. 22–35, 2017.
- [10] C. Aydogdu *et al.*, "Radar interference mitigation for automated driving: Exploring proactive strategies," *IEEE Signal Process. Mag.*, vol. 37, no. 4, pp. 72–84, Jul. 2020.
- [11] A. N. Ramesh *et al.*, "Landmark-based RADAR SLAM for autonomous driving," in *2021 21st International Radar Symposium (IRS)*, 2021, pp. 1–10.
- [12] P. Fritsche *et al.*, "Fusing LiDAR and radar data to perform SLAM in harsh environments," in *Informatics in Control, Automation and Robotics: 13th International Conference, ICINCO 2016 Lisbon, Portugal, 29-31 July, 2016*. Springer, 2018, pp. 175–189.
- [13] D. C. Herraiz *et al.*, "Radar-only odometry and mapping for autonomous vehicles," in *2024 IEEE International Conference on Robotics and Automation (ICRA)*, 2024, pp. 10275–10282.
- [14] H. Zhang *et al.*, "Metaradar: Multi-target detection for reconfigurable intelligent surface aided radar systems," *IEEE Transactions on Wireless Communications*, vol. 21, no. 9, pp. 6994–7010, 2022.
- [15] X. Shao *et al.*, "Target sensing with intelligent reflecting surface: Architecture and performance," *IEEE Journal on Selected Areas in Communications*, vol. 40, no. 7, pp. 2070–2084, 2022.
- [16] X. Song *et al.*, "Intelligent reflecting surface enabled sensing: Cramér-Rao bound optimization," *IEEE Transactions on Signal Processing*, vol. 71, pp. 2011–2026, 2023.
- [17] Z. Xie *et al.*, "RIS-aided radar for target detection: Clutter region analysis and joint active-passive design," *IEEE Transactions on Signal Processing*, pp. 1–16, 2024.
- [18] K. Meng *et al.*, "Intelligent reflecting surface enabled multi-target sensing," *IEEE Transactions on Communications*, vol. 70, no. 12, pp. 8313–8330, 2022.
- [19] H. Kim *et al.*, "RIS-aided monostatic sensing and object detection with single and double bounce multipath," in *2023 IEEE International Conference on Communications Workshops (ICC Workshops)*, 2023, pp. 1883–1889.
- [20] S. Buzzi *et al.*, "Foundations of MIMO radar detection aided by reconfigurable intelligent surfaces," *IEEE Transactions on Signal Processing*, vol. 70, pp. 1749–1763, 2022.
- [21] Y. Huang *et al.*, "Joint localization and environment sensing by harnessing NLOS components in RIS-aided mmwave communication systems," *IEEE Transactions on Wireless Communications*, vol. 22, no. 12, pp. 8797–8813, 2023.
- [22] R. Liu *et al.*, "Integrated sensing and communication with reconfigurable intelligent surfaces: Opportunities, applications, and future directions," *IEEE Wireless Communications*, vol. 30, no. 1, pp. 50–57, 2023.
- [23] W. Lu *et al.*, "Target detection in intelligent reflecting surface aided distributed MIMO radar systems," *IEEE Sensors Letters*, vol. 5, no. 3, pp. 1–4, 2021.
- [24] K. Keykhosravi *et al.*, "RIS-enabled self-localization: Leveraging controllable reflections with zero access points," in *Proc. IEEE Int. Conf. Commun. Workshops (ICC)*, Seoul, South Korea, May 2022.
- [25] H. Kim *et al.*, "RIS-enabled and access-point-free simultaneous radio localization and mapping," *IEEE Transactions on Wireless Communications*, vol. 23, no. 4, pp. 3344–3360, 2024.
- [26] K. Keykhosravi *et al.*, "Leveraging RIS-enabled smart signal propagation for solving infeasible localization problems: Scenarios, key research directions, and open challenges," *IEEE Vehicular Technology Magazine*, vol. 18, no. 2, pp. 20–28, 2023.
- [27] S. Basharat *et al.*, "Reconfigurable intelligent surfaces: Potentials, applications, and challenges for 6G wireless networks," *IEEE Wireless Communications*, vol. 28, no. 6, pp. 184–191, 2021.
- [28] H. Chen *et al.*, "RISs and sidelink communications in smart cities: The key to seamless localization and sensing," *arXiv preprint arXiv:2301.03535*, 2023.
- [29] S. Rao, "Introduction to mmwave sensing: FMCW radars," *Texas Instruments (TI) mmWave Training Series*, pp. 1–11, 2017.
- [30] S. Semiconductors, "Evaluation kit EVK06002." [Online]. Available: <https://www.sivers-semiconductors.com/5g-millimeter-wave-mmwave-and-satcom/wireless-products/evaluation-kits/evaluation-kit-evk06002>
- [31] Z. Zhang *et al.*, "Active RIS vs. passive RIS: Which will prevail in 6G?" *IEEE Transactions on Communications*, vol. 71, no. 3, pp. 1707–1725, 2023.
- [32] E. Grossi *et al.*, "Radar target detection and localization aided by an active reconfigurable intelligent surface," *IEEE Signal Processing Letters*, vol. 30, pp. 903–907, 2023.
- [33] M. Rihan *et al.*, "Spatial diversity in radar detection via active reconfigurable intelligent surfaces," *IEEE Signal Processing Letters*, vol. 29, pp. 1242–1246, 2022.
- [34] P. Fenske *et al.*, "Self-interference leakage estimation 'N'cancellation element: Design of an active self-interference cancellation coupler," *IEEE Microw. Mag.*, vol. 24, no. 6, pp. 68–75, 2023.